Hole-concentration-induced transformation of the magnetic and orbital structures in $Nd_{1-x}Sr_xMnO_3$

R. Kajimoto and H. Yoshizawa
Neutron Scattering Laboratory, ISSP, University of Tokyo, Tokai, Ibaraki 319-1106, Japan

H. Kawano*
The Institute of Physical and Chemical Research (RIKEN), Wako, Saitama 351-0198, Japan

H. Kuwahara[†]
Joint Research Center for Atom Technology (JRCAT), Tsukuba, Ibaraki 305-8562, Japan

Y. Tokura
Joint Research Center for Atom Technology (JRCAT), Tsukuba, Ibaraki 305-8562, Japan
and Department of Applied Physics, University of Tokyo, Bunkyo-ku, Tokyo 113-8656, Japan

K. Ohoyama and M. Ohashi[‡]
Institute for Materials Research, Tohoku University, Sendai 980-77, Japan

We have peformed neutron diffraction measurements on melt-grown polycrystalline samples of $Nd_{1-x}Sr_xMnO_3$ ($0.49 \leqslant x \leqslant 0.75$). A systematic transformation of the crystalline and magnetic structures of this system was observed. This can be consistently explained by the change of the character of the Mn e_g orbitals. When increasing x, the $Nd_{1-x}Sr_xMnO_3$ system exhibits an evolution from a metallic ferromagnetic state, to a metallic A-type antiferromagnetic (AFM), and then to an insulating C-type AFM state. The CE-type charge-ordered AFM state was observed only in the vicinity of $x = 1/2$ and it coexists with the A-type AFM state for $x \gtrsim 1/2$, indicating that the energy difference between these two states is very small. We also found that the MnO_6 octahedra are apically compressed in the CE-type and A-type AFM states due to the $d(3x^2 - r^2)/d(3y^2 - r^2)$ or $d(x^2 - y^2)$ orbital ordering, whereas they are apically elongated by the rod-type $d(3z^2 - r^2)$ orbital ordering in the C-type AFM state. Finally, a selective broadening of Bragg peaks was observed in the C-type AFM phase and its x dependence strongly suggests the onset of charge ordering for either $x = 4/5$ or $x = 3/4$. [S0163-1829(99)11737-5]

I. INTRODUCTION

The systematic investigation of the phase diagram of the perovskite manganites was initially performed on $La_{1-x}Ca_xMnO_3$ in the 1950s.[1,2] A similarly rich phase diagram was reported for $Pr_{1-x}Ca_xMnO_3$ later in the 1980s.[3] The distinctive metallic ferromagnetic (FM) state in these phase diagrams was explained in terms of the double-exchange (DE) mechanism between the e_g electrons of Mn ions, and the richness of the phase diagrams was interpreted as a manifestation of the strong coupling among the spin, charge, and the Jahn-Teller (JT) lattice distortions.

The recent discovery of the colossal magnetoresistance (CMR) effect in the doped perovskite manganites has renewed interest in these compounds, and many experimental and theoretical efforts have been devoted to clarify the origin of this effect. In particular, recent studies have revealed that in addition to the DE interactions and the JT distortions, the ordering of the twofold e_g orbitals of the Mn ions plays an essential role in determining the physical properties in the hole-doped manganites.[4–9] For example, it was recently reported that the underlying $d(x^2 - y^2)$-type orbital ordering leads to a metallic antiferromagnetic (AFM) state instead of

the more common metallic FM or the so-called CE-type charge/spin ordered insulating states.

In view of these developments, it would be extremely useful to perform systematic experimental studies of the hole-concentration dependence of the phase diagrams of these materials to gain a further insight of the interplay between the e_g orbitals and the magnetic, as well as transport properties in the doped manganites. For this purpose we chose $Nd_{1-x}Sr_xMnO_3$ because detailed transport studies have already been performed on this system.[10–12] We carried out comprehensive neutron diffraction studies on melt-grown polycrystalline samples of this system with Sr ion concentrations of $x = 0.49$, 0.50, 0.51, 0.55, 0.60, 0.63, 0.67, 0.70, and 0.75. We will show that the moderately narrow one-electron bandwidth of these materials yields a variety of physical behaviors such as charge ordering, metal-insulator transitions, and unique magnetic structures. We will argue that these result from the interplay between the charge and/or orbital orderings and spin/lattice structures.

First we will show that there is a systematic change in the magnetic structure of $Nd_{1-x}Sr_xMnO_3$ as a function of the hole concentration x. Upon hole doping the ground-state spin ordering varies from that of a metallic ferromagnet to that of the charge-ordered CE-type antiferromagnet, to that of a me-
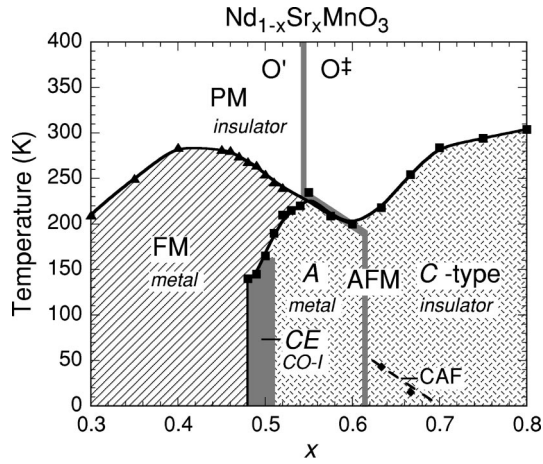
FIG. 1. Phase diagram of $Nd_{1-x}Sr_xMnO_3$ (Ref. 12). Each phase is denoted by capitalized labels; PM: paramagnetic insulating, FM: ferromagnetic, AFM: antiferromagnetic, CO-I: charge-ordered insulator, CE: CE-type charge/spin order, A: A-type antiferromagnetic order, C: C-type antiferromagnetic order, CAF: possible canted antiferromagnetic order.

tallic A-type antiferromagnet, and finally to that of an insulating C-type antiferromagnet ($F \rightarrow CE \rightarrow A \rightarrow C$) (see Fig. 1). It can be shown that each of these spin structures is related to a specific type of orbital ordering, and that the respective crystal structures are also consistent with these. For example, the structures of the CE-type and A-type AFM states are characterized by apically compressed MnO_6 octahedra, while that of the C-type AFM state is characterized by apically elongated octahedra, reflecting their respective layered-type or rod-type orbital ordering patterns (see Fig. 4). These systematic changes of the ordering of the spins and orbitals are well reproduced by recent theoretical calculations that take into account the double degeneracy of the e_g orbitals.[5]

Charge ordering also plays an important role in $Nd_{1-x}Sr_xMnO_3$.[8,10] The CE-type charge/spin order is formed in this system only in a very narrow region of x around $x = 1/2$, and it coexists with the A-type AFM state for $x = 1/2$ and $x = 0.51$. The coexistence of these two states may be interpreted as the orbital-order induced phase segregation between the insulating charge-ordered and the metallic orbital-ordered states. In the C-type AFM phase with x beyond 0.6, the Bragg peaks show a selective anisotropic broadening, indicating disorder in the spacing of the lattice planes along the tetragonal c axis. We will argue that this result suggests a possible charge ordering for a commensurate hole concentration of either $x = \frac{3}{4}$ or $\frac{4}{5}$. The broadening is the result of both the $d(3z^2 - r^2)$-type orbital ordering and the charge ordering.

The rest of this paper is organized as follows. Section II briefly describes the experimental procedures. The experimental results are described in Sec. III, where the property of the magnetic and crystal structures in the $Nd_{1-x}Sr_xMnO_3$ system are discussed with the results of Rietveld refinement analysis. In Sec. IV, the relationships between the magnetic and crystal structures are discussed in detail for each type of the AFM structures. A brief summary is given in Sec. V.

II. EXPERIMENTAL PROCEDURES

The samples used in the present study were prepared by powdering melt-grown single crystals and by pressing them into rod shapes. The single crystals were grown by the floating-zone method. The detailed procedures of the sample preparation have already been described elsewhere.[8,13] The quality of the samples was checked by x-ray diffraction measurements and by inductively coupled plasma mass spectroscopy (ICP). The results of these measurements showed that all of our samples consist of a single crystallographic phase and that the hole concentrations agree with the nominal concentrations within 1%.

Neutron diffraction measurements were performed at the powder diffractometer HERMES and at the triple axis spectrometer GPTAS both installed at the JRR-3M research reactor at the Japan Atomic Energy Research Institute in Tokai, Japan. The incident neutron wavelengths of HERMES and GPTAS were $\lambda = 1.8196$ Å and 2.35 Å, respectively. The collimations of HERMES were $6'$-open-$18'$, while several combinations of the collimators were utilized at GPTAS, depending on the need for intensity or momentum resolution. Most of the measurements made for the structural analysis were performed on HERMES, while most of the measurements of the magnetic reflections were performed on GPTAS because of its higher neutron flux. The samples were mounted in sealed aluminum capsules filled with helium gas, and were attached to the cold head of a closed-cycle helium gas refrigerator. The temperature was controlled within an accuracy of 0.2 K. To obtain the structural parameters, the Rietveld analysis was performed on the powder diffraction data using the analysis program RIETAN.[14]

III. MAGNETIC AND CRYSTAL STRUCTURES

We begin with the description of the overall features of the lattice and magnetic structures of the $Nd_{1-x}Sr_xMnO_3$ system by examining the x-T phase diagram for $0.3 \lesssim x \lesssim 0.8$ shown in Fig. 1.[12] In the distorted perovskite crystal structure, the Mn ions are surrounded by six O ions, and the MnO_6 octahedra form a pseudocubic lattice with Nd or Sr ions occupying its body-centered position. Due to the buckling of the octahedra, however, the unit cell becomes orthorhombic with dimensions $\approx \sqrt{2} \times \sqrt{2} \times 2$ of the cubic cell. There are two orthorhombic phases in the region of interest. One is the well-known O' phase with $c/\sqrt{2} < b < a$,[15] which appears in the lower Sr concentration region for $x \lesssim 0.55$ at room temperature. The other is a pseudotetragonal $O^{\ddagger}$ phase with $a \simeq b < c/\sqrt{2}$ for $x \gtrsim 0.55$ as indicated in Fig. 1. At low temperatures, on the other hand, the region of the O' phase expands, and the phase boundary shifts towards around $x = 0.60$. In addition, a monoclinic structure was detected near the low-temperature structural phase boundary near $x \sim 0.60$. For $0.55 \lesssim x \lesssim 0.60$, a structural transition from the O' phase to the $O^{\ddagger}$ phase coincides with the AFM transition temperature T_N.

For $x < 0.48$, the ground state is a FM metal. In the region for $0.50 \lesssim x \lesssim 0.60$, there is a metallic AFM phase with the layered A-type spin structure.[1] When x is further increased there is another AFM phase but with the C-type spin structure in the $O^{\ddagger}$ phase. In this phase, the resistivity uniformly
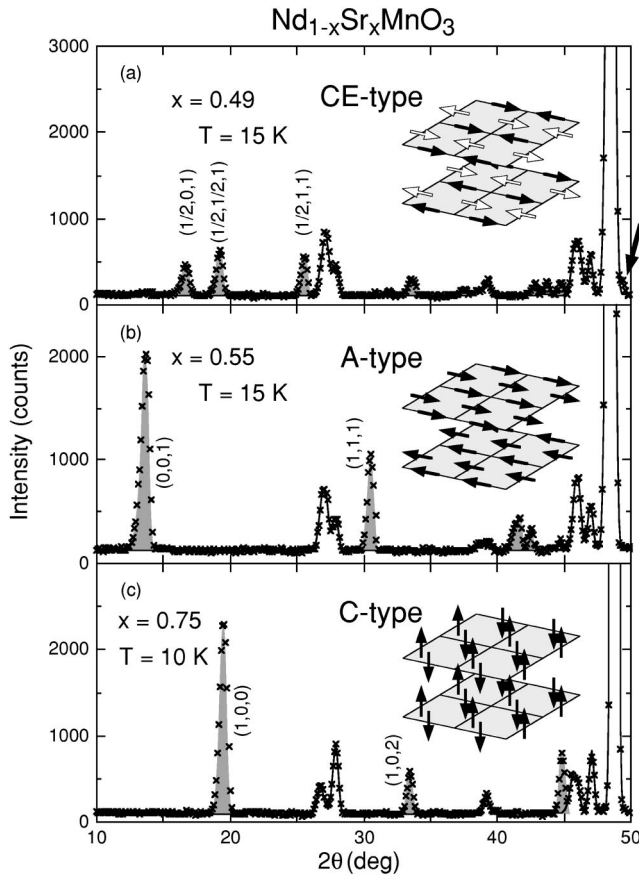
FIG. 2. Low scattering angle portion of the powder diffraction patterns for (a) $x = 0.49$ at 15 K, (b) $x = 0.55$ at 15 K, and (c) $x = 0.75$ at 10 K collected at HERMES. The solid lines are the calculated intensities for the nuclear reflections, and the hatched peaks represent the AFM Bragg reflections. The insets show the spin patterns for each AFM structure. For the *CE*-type AFM structure the black and white arrows denote the spins of the Mn^{3+} and Mn^{4+} sites, respectively. A solid arrow in the panel (a) indicates the superlattice peak corresponding to the lattice distortion due to the *CE*-type charge ordering.

increases with lowering temperature, and the sample remains insulating at all temperatures, although the temperature derivative of the resistivity shows an anomaly at T_N.[12] In a very narrow region of Sr concentration around $x \sim 0.50$ the system exhibits two low-temperature transitions, first to an intermediate metallic FM phase below T_C and then to a charge-ordered insulating phase which is accompanied with the *CE*-type AFM spin structure.

A. Magnetic structures

The AFM spin ordering yields superlattice reflections in the neutron diffraction profiles and from these the spin structure of the material being studied can be normally determined. In Fig. 2, we show typical powder diffraction patterns for $Nd_{1-x}Sr_xMnO_3$ ($x = 0.49$, 0.55, and 0.75) measured at low temperatures (~ 10 K). One can clearly recognize the different superlattice reflection patterns for the *CE*-type, *A*-type, and *C*-type AFM spin arrangements, respectively. The cross symbols represent the measured intensities, and the solid lines are the calculated diffraction patterns for the

nuclear reflections obtained by the Rietveld analysis. The AFM superlattice reflections are indicated by hatches, and the corresponding spin ordering patterns are depicted in the insets.

The CE-type spin ordering [Fig. 2(a)] is characterized by the alternate ordering of the Mn^{3+} and Mn^{4+} ions. The spin ordering pattern in the *ab* plane is rather complicated and these planes stack antiferromagnetically along the *c* axis. The magnetic reflections for the Mn^{3+} and Mn^{4+} sublattices are decoupled. The characteristic reflections for the Mn^{3+} sublattice can be indexed as $(h/2,k,l)$ with $k =$ integer and $h,l =$ odd integer, while the Mn^{4+} sublattice reflections are indexed as $(h/2,k/2,l)$ with $h,k,l =$ odd integer.

In the *A*-type spin ordering [Fig. 2(b)] the spins typically order ferromagnetically in the *ab* plane with the moments pointing toward the *a* axis, and the FM planes are stacked antiferromagnetically along the *c* axis. The magnetic reflections appear at (hkl) with $h + k =$ even integer and $l =$ odd integer. An exception to this occurs for the monoclinic lattice (as in the case for $x = 0.60$) where the *A*-type AFM phase is characterized by FM planes stacked along the [110] direction. This has also been observed in the monoclinic $Pr_{1/2}Sr_{1/2}MnO_3$.[8]

In the *C*-type spin ordering [Fig. 2(c)], the spins order ferromagnetically along the *c* axis while the neighboring spins in the *ab* plane point the opposite direction. The magnetic reflections are observed at (hkl) with $h + k =$ odd integer and $l =$ even integer.

We note that, for the $x = 0.63$ and 0.67 samples, an additional FM component was observed in the magnetization curves below $T_{CA} \sim 45$ K for the $x = 0.63$ sample or $T_{CA} \sim 15$ K for the $x = 0.67$ sample,[12] as indicated by the line CAF in Fig. 1. To confirm the existence of the FM component in these samples, we have measured the temperature dependence of the (110) and (002) reflections for the $x = 0.63$ sample. If FM Bragg scattering appears, the intensity of these reflections should increase below a characteristic transition temperature. Although we have observed a slight increase of the intensity below T_{CA}, the magnitude of this increase is within the statistical error. We conclude that if such FM component exists it is too weak for powder diffraction data to accurately determine the magnitude of the magnetic moment.

In Table I, we summarize the magnetic moments per Mn site and their directions for all the samples studied. Interestingly, we found a clear trend that the direction of the moment is always parallel to the longest lattice axis (see Table II).

B. Crystal structures

In order to characterize the crystal structure of each phase, we have performed the Rietveld analysis on neutron powder diffraction patterns for all the samples observed at selected temperatures. The obtained structural parameters are summarized in Table II. The types of the crystal structure (CS) and of the magnetic structure (MS) are also listed in the table. The shapes of MnO_6 octahedra for the O' and $O^{\ddagger}$ phases are schematically illustrated in Figs. 3(a) and (b), respectively. Below we examine the characteristic crystal symmetries for each phase, and the distortion of the MnO_6 octahedra.

TABLE I. Magnetic structure (MS), magnetic moments, and their directions. For the CE-type AFM structure, the magnetic moments are shown for both Mn^{3+} and Mn^{4+} sites. The directions of the moments for the two sites were determined to be identical within the experimental accuracy.

x	T (K)	MS	Moment/Mn (μ_B)	
0.49	15	CE	2.9, 2.6	[100]
		F	0.8 [a]	
	160	F	2.6	[100]
0.50	10	CE	3.0, 2.7	[100]
0.51	10	A	2.4	[100]
		CE	1.7, 1.5	[100]
	210	F	1.9	[100]
0.55	15	A	3.0	[100]
0.63	10	C	2.8	[001]
0.67	10	C	2.8	[001]
0.75	12	C	2.9	[001]

[a]Derived from the magnetization curve in Ref. 12.

In spite of the fact that many orthorhombic perovskite manganites have the $Pbnm$ ($Pnma$ in another setting) symmetry due to the $GdFeO_3$-type distortion, the measured powder diffraction profiles in the O' phase were well fitted with the orthorhombic space group $Ibmm$ (or $Imma$). It should be noted that the $Ibmm$ structure was also observed in $Pr_{0.65}Ba_{0.35}MnO_3$ at room temperature (Ref. 16), $Nd_{0.5}Sr_{0.5}MnO_3$ (Ref. 17), and $Pr_{1/2-x}Y_xSr_{1/2}MnO_3$ (Ref.

18). To see the difference of the two structures, the tilts of the MnO_6 octahedra for $Pbnm$ and $Ibmm$ are illustrated in Fig. 3(c). In the $Pbnm$ symmetry, the octahedra rotate around both the b and c axis. In contrast, the tilting of the octahedra is restricted only to the b axis in the $Ibmm$ symmetry, and thereby the x and y coordinates of the in-plane oxygen O(2) are fixed to 1/4. As a result, two Mn–O bonds in the ab plane have an equal length.

In principle one can distinguish the $Ibmm$ from the $Pbnm$ symmetry. Because $Pbnm$ has a lower symmetry than $Ibmm$ there should be some Bragg reflections that are allowed only in the $Pbnm$ symmetry. In the paramagnetic phase, however, we observed no such additional reflections that would be specific to the $Pbnm$ symmetry, and therefore we tentatively assigned the space group in the paramagnetic phase as $Ibmm$. Unfortunately, the scattering angles of AFM superlattice reflections overlap with the $Pbnm$ specific reflections in the low-temperature AFM phase, and this prevented us from determining the precise space group in this phase. Furthermore, we have performed Rietveld analysis for both space groups, and obtained almost identical R factors. For comparison, the two parameter sets determined for both symmetries on the $x=0.50$ sample are shown in Table II, but only the parameter sets for the $Ibmm$ symmetry are tabulated for the rest of the samples.

We found that the measured powder diffraction profiles in the $O^{\ddagger}$ phase were well fitted using the tetragonal space group $I4/mcm$. $Pr_{0.65}Ba_{0.35}MnO_3$ at 210 K (Ref. 16) and $La_{0.5}Sr_{0.5}MnO_3$ (Ref. 19) were also reported to have the
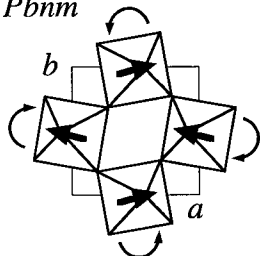
(a) O' ($x \sim 0.5$; CE-type, A-type) $Ibmm$ ($Pbnm$)
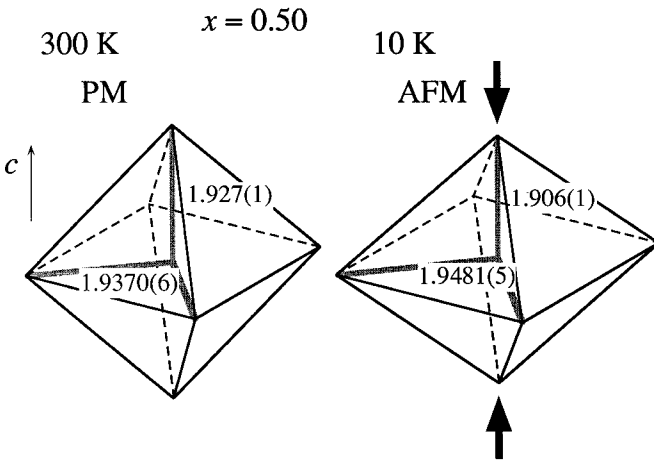
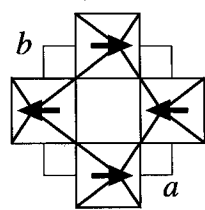(b) O‡ ($x > 0.6$; C-type) $I4/mcm$
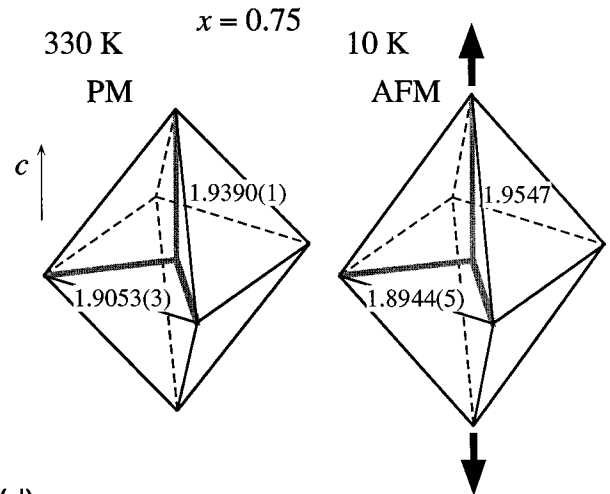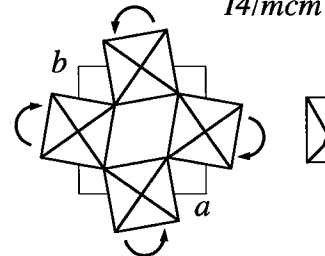

FIG. 3. Schematic picture of the MnO_6 octahedra (a) in the O' phase and (b) in the $O^{\ddagger}$ phase for the paramagnetic and low-temperature AFM phases. (c), (d) Rotation patterns in the basal plane for each of the designated structures. For the $I4/mcm$ structure (d), the projection of the octahedra onto one of the [110] planes is also depicted in the right panel.

TABLE II. Lattice constants, Mn–O bond lengths, and Mn–O–Mn bond angles determined from the Rietveld analysis of the powder profiles. CS denotes the crystal structure and the meaning of the symbols O' and $O^{\ddagger}$ is described in Sec. III. The column MS lists magnetic structures for all samples: the symbols P, F, CE, A, and C denote the PM, FM, CE-type AFM, A-type AFM, and C-type AFM structures, respectively. d_c and d_{ab} denote the Mn–O bond lengths along the c axis and within the ab plane. Θ_c and Θ_{ab} denote the Mn–O–Mn bond angles along the c axis and within the ab plane. For $x=0.50$, the parameters obtained by the analysis in the $Pbnm$ symmetry are also indicated. For $x=0.70$ at 10 K and $x=0.75$ at 10 K, two values for $c/\sqrt{2}$ and d_c are shown because the structure parameters were analyzed according to the two phase model as described in Sec. VI A. RT indicates room temperature.

x	T (K)	CS	MS	a (Å)	b (Å)	$c/\sqrt{2}$ (Å)	d_c (Å)	d_{ab} (Å)		Θ_c (deg)	Θ_{ab} (deg)
0.49	15	O'	CE	5.5129(3)	5.4409(3)	5.3198(3)	1.907(1)	1.9491(5)		160.9(4)	166.9(2)
	160	O'	F	5.4645(3)	5.4174(3)	5.3942(3)	1.927(1)	1.9355(6)		163.7(5)	167.4(3)
	320	O'	P	5.4727(3)	5.4286(3)	5.3978(3)	1.928(1)	1.9379(6)		163.6(5)	167.9(3)
0.50	10	O'	CE	5.5114(4)	5.4400(4)	5.3160(4)	1.906(1)	1.9481(5)		160.8(4)	167.2(3)
		in the $Pbnm$ symmetry		5.5113(4)	5.4400(4)	5.3160(4)	1.907(1)	1.92(2)	1.98(2)	160.8(4)	167.0(3)
	300	O'	P	5.4726(4)	5.4265(4)	5.3900(4)	1.927(1)	1.9370(6)		163.1(5)	168.2(3)
		in the $Pbnm$ symmetry		5.4726(4)	5.4264(4)	5.3910(4)	1.927(1)	1.93(4)	1.95(4)	163.1(4)	168.1(3)
0.51	10	O'	$A+CE$	5.5075(3)	5.4441(2)	5.3131(2)	1.902(1)	1.9472(4)		161.9(4)	167.7(2)
	160	O'	A	5.4999(3)	5.4446(3)	5.3242(2)	1.905(1)	1.9453(4)		162.3(4)	168.1(2)
	210	O'	F	5.4697(3)	5.4226(3)	5.3840(3)	1.923(1)	1.9358(4)		163.7(4)	168.2(3)
	300	O'	P	5.4718(3)	5.4281(3)	5.3903(3)	1.925(1)	1.9368(5)		164.0(5)	168.4(3)
0.55	15	O'	A	5.4906(3)	5.4385(3)	5.3075(3)	1.896(1)	1.9414(5)		163.6(5)	168.7(3)
	300	$O^{\ddagger}$	P	5.3903(2)	5.3903(2)	5.4999(2)	1.9445(1)	1.9218(5)		180	165.2(2)
0.60	10	M	A	5.365(2)	5.367(2)	5.4964(4)	2.01(3)	1.87(6)	1.90(6)	180	165.0(7)
					$\beta=91.225(3)°$		1.88(3)	1.92(6)	1.96(6)		166.3(7)
	300	$O^{\ddagger}$	P	5.3782(2)	5.3782(2)	5.5027(2)	1.9455(1)	1.9162(9)		180	165.8(4)
0.63	10	$O^{\ddagger}$	C	5.3236(2)	5.3236(2)	5.5633(2)	1.9669(1)	1.9009(4)		180	163.9(2)
	RT	$O^{\ddagger}$	P	5.3737(2)	5.3737(2)	5.5067(2)	1.9469(1)	1.9139(8)		180	166.1(4)
0.67	10	$O^{\ddagger}$	C	5.3190(2)	5.3190(2)	5.5588(3)	1.9653(1)	1.898(1)		180	164.4(4)
	300	$O^{\ddagger}$	P	5.3637(3)	5.3637(3)	5.5005(3)	1.9447(1)	1.9085(9)		180	167.1(5)
0.70	10	$O^{\ddagger}$	C	5.3222(3)	5.3222(3)	5.5603(4)	1.9659(1)	1.8968(5)		180	165.5(2)
						5.5387(6)	1.9582(2)				
	RT	$O^{\ddagger}$	P	5.3625(3)	5.3625(3)	5.5034(3)	1.9457(1)	1.9060(7)		180	168.2(4)
0.75	10	$O^{\ddagger}$	C	5.3243(4)	5.3243(4)	5.5432(3)	1.9598(1)	1.8944(5)		180	167.1(3)
						5.5144(4)	1.9496(2)				
	330	$O^{\ddagger}$	P	5.3717(2)	5.3717(2)	5.4843(3)	1.9390(1)	1.9053(3)		180	170.8(2)

same space group. The main features of $I4/mcm$ are also shown in Fig. 3(d). In this symmetry the MnO_6 octahedra rotate only around the c axis, and all the Mn–O bonds in the ab plane are equal in length. The octahedra in the $z=1/2$ plane rotate in the opposite directions to those in the $z=0$ plane.

As illustrated in Figs. 3(c) and (d), the observed orthorhombic and tetragonal structures are closely related. If each space group is denoted by the tilting of the MnO_6 octahedra in Glazer's terminology,[20] the $Pbnm$, $Ibmm$, and $I4/mcm$ symmetries are expressed by $a^+b^-b^-$, $a^0b^-b^-$, and $a^0a^0c^-$, respectively. The positive and negative superscripts denote that the octahedra are tilted either in-phase or antiphase along the tilt axis, and the 0 superscript means that there is no tilt.[20] Therefore, these structures can be derived from the cubic lattice by introducing successive tilts of the MnO_6 octahedra. Comparing the projection of the octahedra onto the [001] plane in the orthorhombic phase [Fig. 3(c)] and onto the [110] plane in the tetragonal phase [right part of

Fig. 3(d)], one can see that, as far as the tilting of the octahedra is concerned, the tetragonal axis [001] coincides with the [110] axis in the orthorhombic structure.

In addition to the tilting, the distortions of the MnO_6 octahedra also provide useful information on the orbital as well as charge ordering. As one can see from Table II, the two Mn–O bonds in the ab plane are always longer than those along the c axis in the O' phase. This feature indicates that the A-type AFM structure is accompanied with the $d(x^2-y^2)$-type orbital order as depicted in Fig. 4(b), and this result is supported by recent theoretical calculations.[5] This type of orbital order causes unique magnetic and transport properties due to the strongly anisotropic coupling within and perpendicular to the orbital ordered planes. As we have predicted and demonstrated in previous studies (see Sec. V),[8,11,12,27] this type of orbital order yields a *metallic A*-type AFM state. It should be noted that one might expect that the orbital-order-induced anisotropy will be significantly smaller in the paramagnetic phase, since the difference of the bond
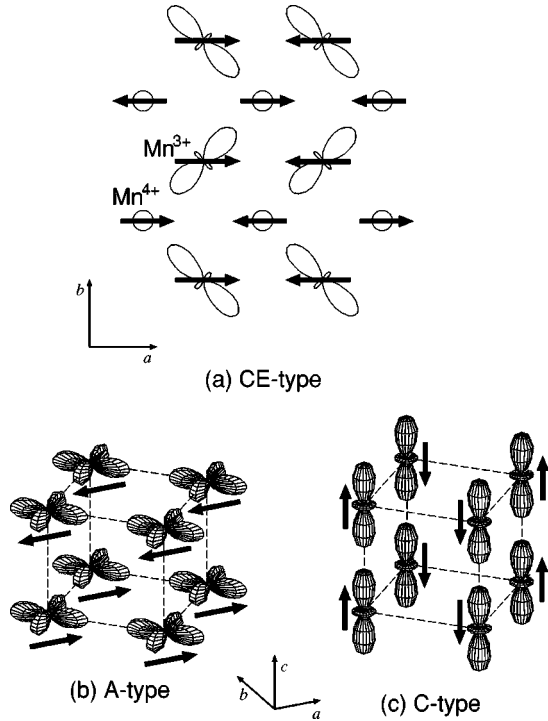
FIG. 4. Schematic picture of the ordering of the e_g orbitals in the various AFM phases. (a) CE-type, (b) A-type, and (c) C-type, respectively. The directions of the spins are represented by arrows.

lengths between the apical and in-plane Mn–O bonds becomes rather small at elevated temperatures. Surprisingly, however, the anisotropic behavior persists in the high-temperature phases. Recently, we have demonstrated the existence of the anomalous anisotropic spin fluctuations in the paramagnetic and FM phases in $Nd_{0.50}Sr_{0.50}MnO_3$,[9] indicating that the $d(x^2-y^2)$-type orbital order has strong influence even at high temperatures.

In the $O^{\ddagger}$ phase, on the other hand, the Mn–O bond length along the c axis is longer than the ones in the ab plane, and this difference is further enhanced in the AFM phase. The apically stretched MnO_6 octahedron is consistent with the ordering of the $d(3z^2-r^2)$ orbitals depicted in Fig. 4(c). Recent theoretical calculations have confirmed that there seems to be a correspondence between the C-type AFM state with the ordering of the $d(3z^2-r^2)$ orbitals in the higher doping region.[5]

Finally, we would like to mention the CE-type charge/orbital ordering. This type of ordering is characterized by the alternate ordering of the Mn^{3+} and Mn^{4+} ions and by the ordering of the $d(3x^2-r^2)/d(3y^2-r^2)$ orbitals on the Mn^{3+} sites in the ab plane as depicted in Fig. 4(a). This type of orbital ordering doubles the size of the unit cell along the b axis, and produces superlattice reflections at $(h,k/2,l)$ with $h=$ even, $k=$ odd, and $l=$ integer. We observed superlattice reflections in the $x=0.49$ and 0.50 samples at $2\theta=49°$ [indicated by an arrow in Fig. 2(a)] that can be indexed as $(2\frac{1}{2}2)+(2\frac{3}{2}0)$, as previously observed for $Pr_{1-x}Ca_xMnO_3$.[3]

In the CE-type charge ordering there are two independent Mn sites for the Mn^{3+} and Mn^{4+} ions and we need to consider two type of distortions of the MnO_6 octahedra. Clearly such an analysis multiplies the number of parameters in a fitting process, resulting in a less reliable determination of

the structural parameters. For this reason we omitted this doubling of the unit cell and performed the Rietveld analysis on the CE-type samples assuming only the original $Ibmm/Pbnm$ structure. Consequently, the obtained Mn–O bond lengths and Mn–O–Mn angles give the averaged values for two Mn sites.

IV. INFLUENCE OF THE CE-TYPE ORDERING

Near $x\sim\frac{1}{2}$, the doped perovskite manganites are usually expected to show the CE-type charge/orbital/spin superstructure depicted in Fig. 4(a).[1–3] For $Pr_{1-x}Ca_xMnO_3$, for instance, the CE-type ordering is observed over a wide range of dopings $0.3\lesssim x\lesssim 0.5$.[3,21–23] In the $Nd_{1-x}Sr_xMnO_3$ system, however (see Fig. 1), the CE-type ordering is observed only in a very narrow range near $x\sim0.50$. In particular, note that the CE-type ordering is not observed in the $x=0.55$ sample.[8]

A distinct feature of the CE-type ordering in $Nd_{1-x}Sr_xMnO_3$ is the coexistence with another spin ordering. Because the FM order is taken over by the A-type AFM order near $x=0.5$ (see the phase diagram in Fig. 1), the FM order coexists with the CE-type order in the $x=0.49$ sample, whereas the A-type AFM order coexists with the CE-type order in the $x=0.51$ sample. We will describe the behavior of the $x=0.49$ and 0.51 samples in detail below. Similar results were also recently reported on $Nd_{1-x}Sr_xMnO_3$ for $x=0.52$ and 0.54.[25]

Figure 5 shows the temperature dependence of the magnetic Bragg peak intensities, the lattice constants, and the resistivity for the $x=0.49$ and 0.51 samples. As shown in Fig. 5(a), the intensity of the (110) and (002) reflections increases below $T_C\simeq280$ K indicating FM order below this temperature. Below $T_N\simeq160$ K, this intensity suddenly drops while the $(\frac{1}{2}\frac{1}{2}1)$ reflection appears, indicating the formation of the CE-type AFM order. It should be noted, however, that the bulk magnetization studies strongly suggest the persistence of the ferromagntic order below T_N indicating that the FM order coexists with the CE-type AFM order. As shown in Table I, the $x=0.49$ sample has a FM moment of $0.8\mu_B$ at 15 K.

For the $x=0.51$ sample, the behavior of the magnetic ordering is very similar to that of the $x=0.50$ sample reported in Refs. 8 and 9. As shown in Fig. 5(d), the intensity of the (110)+(002) reflections increases below $T_C\simeq240$ K due to the onset of the FM order. With decreasing temperature, this intensity increases quickly, but shows a sudden drop at $T_N^A\simeq200$ K at which the (001) A-type AFM reflection appears. In contrast to the $x=0.49$ FM sample, the intensity of (110)+(002) reflection in the $x=0.51$ AFM sample has no magnetic contribution below T_N^A. The difference between the intensity above T_C and below T_N^A is due to the structural transition at T_N^A. When lowering the temperature further, the $(\frac{1}{2}\frac{1}{2}1)$ CE-type AFM superlattice reflection appears below $T_N^{CE}\simeq150$ K. Note that the CE-type ordering suppresses the increase of the intensity of the (001) A-type AFM reflection below T_N^{CE}, indicating that the two types of spin ordering are strongly correlated.

The temperature dependence of the lattice constants in the $x=0.49$ sample is shown in Fig. 5(b). This figure shows a
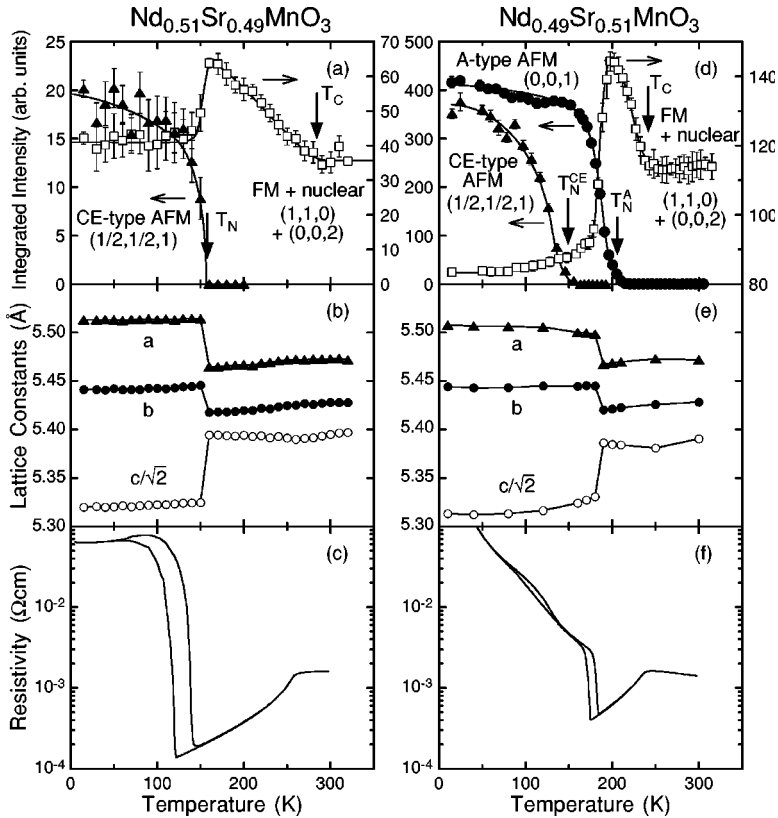
FIG. 5. Temperature dependence of the intensity of the magnetic Bragg peaks, the lattice constants, and the resistivity for the $x=0.49$ FM sample: (a)–(c), and for the $x=0.51$ AFM sample: (d)–(f), respectively. The resistivity data are reproduced from Ref. 12.

weak inflection at T_C and a sharp jump at T_N, where the c axis shrinks and the a and b axes expand. This behavior is consistent with the CE-type orbital ordering in the ab plane. Similarly, the lattice constants of the $x=0.51$ AFM sample exhibit a large split at T_N^A [Fig. 5(e)], indicating that the A-type magnetic transition is accompanied by a structural transition that stabilizes the $d(x^2-y^2)$-type planar orbital ordering as discussed in Sec. III. The lattice constants, however, do not show any distinct anomaly at T_N^{CE}. In fact, we have carried out detailed structural analysis on the two powder diffraction data, one at $T=160$ K in the A-type AFM phase for $T_N^{CE}<T<T_N^A$ and the other at $T=10$ K in the low-temperature phase where two types of ordering coexist. We found no difference in the crystal structures of these two AFM phases (see Table II). In particular, all the nuclear reflections in the powder diffraction data at 10 K can be well fitted to a single structure in spite of the coexistence of the A-type and CE-type AFM ordering. These results on the $x=0.51$ sample demonstrate that the crystal structure of the A-type AFM phase in $Nd_{1-x}Sr_xMnO_3$ is practically indistinguishable from that of the CE-type phase despite the difference in the two spin structures.[26]

The change of the magnetic structure also has a strong influence on the behavior of the resistivity. As shown in Fig. 5(c), the resistivity in the $x=0.49$ FM sample shows metallic behavior below T_C, then a sharp rise at T_N due to the CE-type charge order. The increase of the resistivity is, however, suppressed below ~ 100 K by the FM order with moments of $0.8\mu_B$ that coexist with the CE-type AFM spin order. In the $x=0.51$ AFM sample, on the other hand, the resistivity shows metallic behavior below T_C, a moderate increase at the onset of the A-type AFM spin order, and then a second increase at T_N^{CE} due to the CE-type charge order as shown in

Fig. 5(f). By comparing this behavior with that of the $x=0.49$ FM sample, the influence of the spin ordering is clear. The FM spin order restricts the resistivity of the $x=0.49$ FM sample to the order of $\rho\sim 5\times 10^{-2}$ Ω cm for $T<T_N$. In contrast, the resistivity of the $x=0.51$ sample exhibits a jump at T_N^A, while it remains of the order of $\rho\sim 5\times 10^{-3}$ Ω cm in the metallic A-type AFM phase for $T_N^{CE}<T<T_N^A$, and then increases monotonically below $T<T_N^{CE}$. It should be noted that the metallic resistivity in the A-type AFM state for $T_N^{CE}<T<T_N^A$ in the $x=0.51$ AFM sample is very similar to the results observed in the *metallic* A-type AFM samples.[8,11,12,24,27]

There are several possibilities for the origin of the simultaneous presence of the CE-type ordering and the FM or A-type AFM spin ordering in the $x=0.49$ and 0.51 samples. Scenarios of the inhomogeneous distribution of the holes in the sample or a canted magnetic ordering consisting of the CE-type and A-type moments seem to be consistent with the observed results. The former scenario can be attributed either to an arbitrary concentration distribution, or to an intrinsic phase segregation. Although it is extremely difficult to experimentally distinguish these two possibilities, there are some interesting observations that seem to favor the intrinsic spontaneous phase segregation in doped manganites near $x\sim\frac{1}{2}$.

As mentioned above, the increase of the CE-type Bragg intensity suppresses the A-type AFM intensity in the $x=0.51$ sample; in other words, the CE-type order grows at the expense of the A-type ordered region. This fact excludes the possibility of an arbitrary concentration distribution of the holes. In addition, we found that the magnetic moments for the A-type and CE-type AFM structures lie in the same direction, i.e., along the a axis (Table I). This result seems to
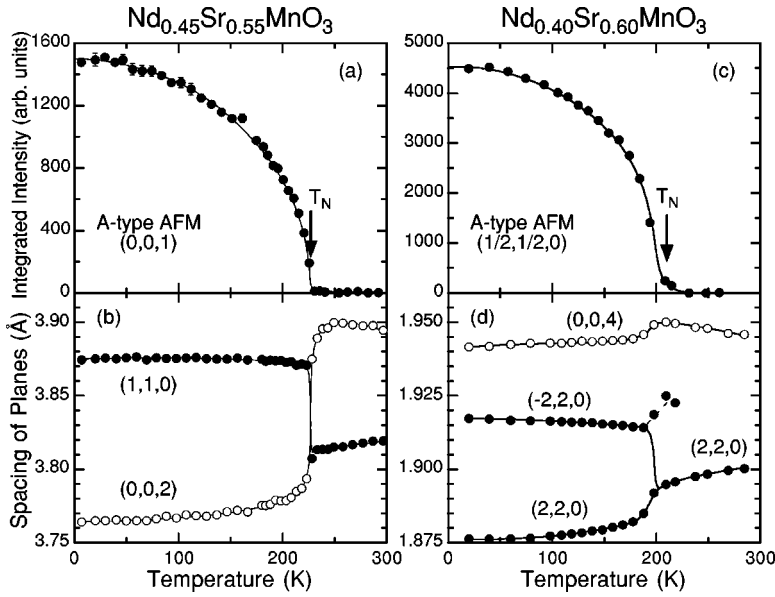
FIG. 6. Temperature dependence of the intensities of the AFM Bragg peaks and the spacings of the lattice planes. (a),(b) (001) AFM Bragg peak and the spacing of (110) and (002) planes for $x=0.55$. (c),(d) the $(\frac{1}{2}\frac{1}{2}0)$ AFM Bragg peak and the spacing of (220) and (004) planes for $x=0.60$.

suggest that a canted magnetic ordering is unlikely in the present case.[28]

In the present study, we found that the averaged lattice structure of the CE-type phase is almost identical with that of the A-type phase. As shown in the case of the $x=0.51$ sample, the lattice parameters exhibit a small anomaly between two phases. Since both phases exhibit orbital ordering within the basal plane, the orbitals are reorganized with surprisingly small lattice distortions from the $d(3x^2-r^2)/d(3y^2-r^2)$-type orbital ordering for the CE-type order, where the charges are localized, to the $d(x^2-y^2)$-type orbital ordering for the A-type AFM order, where the charges are delocalized.

Combining these observations, we believe that the coexistence of two states strongly indicates that these have very similar energies, and that their relative fraction can be easily varied either by temperature or by tuning other physical parameters such as the electron bandwidth. This could also explain why the CE-type ordering appears only in a very narrow concentration range of $1\sim2\%$ around $x=1/2$ in the $Nd_{1-x}Sr_xMnO_3$ system. As discussed in Ref. 30, we argue that this behavior can be viewed as an effective phase separation between two different orbital ordered regions which takes place in doped manganites with hole concentration $x \gtrsim \frac{1}{2}$.

The strong correlation between the coexistence of the CE-type and A-type ordering and their resistivity has also been observed in doped manganite systems with $x=\frac{1}{2}$ including the two-dimensional single and bilayered systems, $La_{0.5}Sr_{1.5}MnO_4$ (Ref. 29) and $La_1Sr_2Mn_2O_7$ (Ref. 30).

V. THE METALLIC A-TYPE ANTIFERROMAGNETIC PHASE

The most important result in the metallic A-type antiferromagnetic phase is the fact that all crystal structures in this phase share the common feature that the lattice spacing in the direction of the AFM stacking is the smallest (see Fig. 3). This salient feature causes an anisotropy in both magnetic and transport properties, as discussed in Sec. III B. As reported recently, the spin-wave dispersion relation in the me-

tallic A-type AFM $Nd_{0.45}Sr_{0.55}MnO_3$ exhibits a large anisotropy of the effective spin stiffness constants between the intraplanar direction within the FM layers and the interplanar direction perpendicular to the layers.[8,27] A similar anisotropy was also observed in the resistivity of the A-type AFM samples.[11,12] This anisotropy is strong evidence of the $d(x^2-y^2)$-type orbital ordering within the FM layers, and is fully consistent with the characteristics of the crystal and magnetic structures observed in the present studies. In this section, we will focus on the detailed crystal structures observed in the region of $0.55 \leq x < 0.63$ where the system shows a transition from the paramagnetic $O^{\ddagger}$ phase to the metallic A-type AFM O' phase.

Figures 6(a) and 6(b) show the temperature dependence of the A-type AFM Bragg peak and the d spacing of the planes of the (110)/(002) doublet for the $x=0.55$ sample. The (001) A-type AFM Bragg peak appears below $T_N=230$ K. The lattice spacings of the (002) and (110) nuclear reflections cross at T_N due to the change of the space group from $O^{\ddagger}$ to O'. The shrinkage of the c axis in the A-type AFM phase reflects the $d(x^2-y^2)$-type orbital ordering.

Figures 6(c) and (d) show the similar temperature dependence for the $x=0.60$ sample. This sample also belongs to the tetragonal $O^{\ddagger}$ phase at the paramagnetic phase, and shows a first-order structural phase transition at T_N. In contrast to the $x=0.55$ sample, however, it has a monoclinic structure whose unique axis is the c axis in the AFM phase, as one can clearly see the splitting of the tetragonal (220) reflection into the monoclinic $(220)+(\bar{2}20)$ reflections below T_N.

We have previously reported that $Pr_{0.50}Sr_{0.50}MnO_3$ is also monoclinic in the A-type AFM phase, and that its crystal structure belongs to the $P112_1/n$ ($P2_1/c$, cell choice 2) space group.[8] In order to analyze the powder patterns of the present $Nd_{0.40}Sr_{0.60}MnO_3$ sample collected at 10 K, we have performed the Rietveld analysis assuming the same $P112_1/n$ space group at first. This choice, however, predicts too many Bragg reflections that are not observed in the diffraction patterns. Therefore, as the next step, we fitted the profile with the space group $I112/m$ ($C2/m$, cell choice 3) which has a
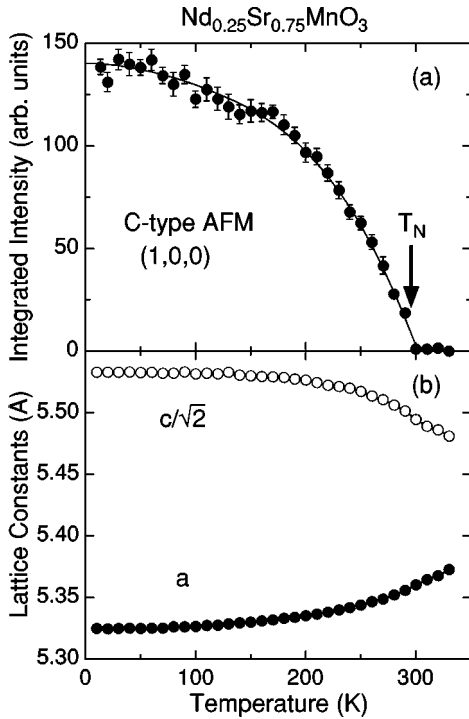
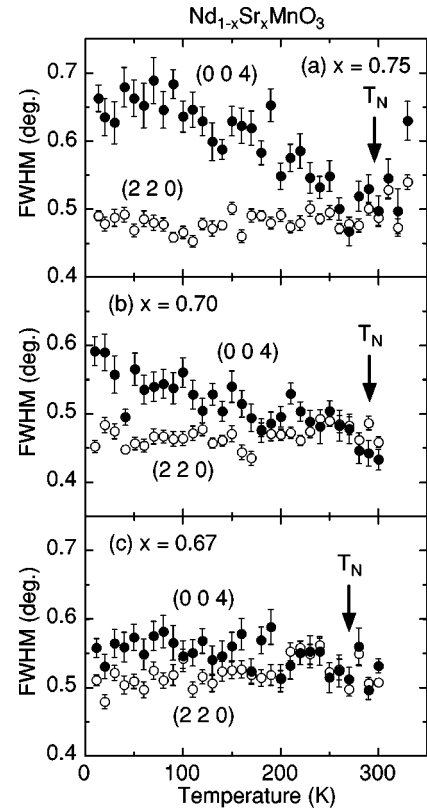FIG. 7. Temperature dependence of the intensities of the AFM Bragg peaks and the lattice constants for $x = 0.75$.

FIG. 8. Temperature dependence of the FWHM of the (004) and (220) reflections for (a) $x = 0.75$, (b) $x = 0.70$, and (c) $x = 0.67$.

higher symmetry, and obtained an agreement almost as good as for the $P112_1/n$ space group. We have listed the parameters obtained with this symmetry in Table II. The difference of the crystal structure of two space groups is the following: In both space groups, two unequal Mn sites are placed at adjacent sites alternately in all directions, but the freedom of the O sites is much more restricted in the case of the $I112/m$ structure. The apical oxygen O(1) is placed on the line that connects the nearest Mn ions along the c axis, and only its z coordinate is allowed to vary, while the position of the in-plane oxygens O(2) and O(3) are confined in the ab plane.

Unfortunately, the quality of the refinement for the $x = 0.60$ sample is the worst among the samples analyzed in the present study ($S = R_{wp}/R_e \simeq 2.2$ for $x = 0.60$ sample, whereas S is less than 2 for the other samples). The main reason for the large R factor may be that this sample is not in a single phase at 10 K, presumably because the AFM phase of $x = 0.60$ lies just at the boundary between the orthorhombic O' and the tetragonal $O^{\ddagger}$ regions.[31] In fact, we have found that $\sim 10\%$ of the sample of the $x = 0.63$ sample has the same lattice constants as those for $x = 0.60$ at 10 K, and shows A-type antiferromagnetism. This large R factor causes a slight ambiguity in the identification of the indices for the closely located peaks such as (004), (220), and ($\bar{2}20$) in the monoclinic phase, but when the assignment of the three axes was assumed to be that of Fig. 6(d), the Rietveld analysis gave the best fit.

The $x = 0.60$ sample exhibits the same A-type AFM structure with the $x = 0.51$ and 0.55 samples. However, the monoclinic structure in the $x = 0.60$ sample affects its magnetic structure. The AFM superlattice reflections in the $x = 0.60$ sample are indexed as $(2n \pm \frac{1}{2}, 2n' \pm \frac{1}{2}, \text{even})$ with n, n' = integer, while those in the $x = 0.51$ and 0.55 samples are indexed as (hkl) with $h + k = $ even integer and $l = $ odd. This

difference in the reflection conditions indicates that the propagation vector of the AFM structure for $x = 0.60$ is different from the other A-type samples. It is rotated by 90° from the [001] axis, and it points towards the [110] direction. This is consistent with the fact that the d spacing of (001) remains larger than that of (110) below T_N in this sample. Such a rotation of the propagation vector of the A-type AFM ordering was also observed in another monoclinic sample $Pr_{0.50}Sr_{0.50}MnO_3$ (Ref. 8).

VI. POSSIBLE CHARGE ORDER IN THE *C*-TYPE AFM INSULATING PHASE

Finally, we shall discuss features of the insulating *C*-type AFM state which appears in the $O^{\ddagger}$ phase for $0.63 \lesssim x$.

A. Anomaly in the lattice constant *c* in the *C*-type AFM phase

Figure 7 shows the temperature dependence of the intensity of the AFM Bragg peak and of the lattice constants for the $x = 0.75$ sample. The (100) AFM Bragg peak for the *C*-type spin ordering was observed below $T_N \simeq 300$ K. The change of the lattice constants with temperature is very smooth throughout T_N, although the difference between the values at 330 K and those at 10 K is quite large. When lowering the temperature, the length of the c axis increases whereas the a (b) axis decreases.
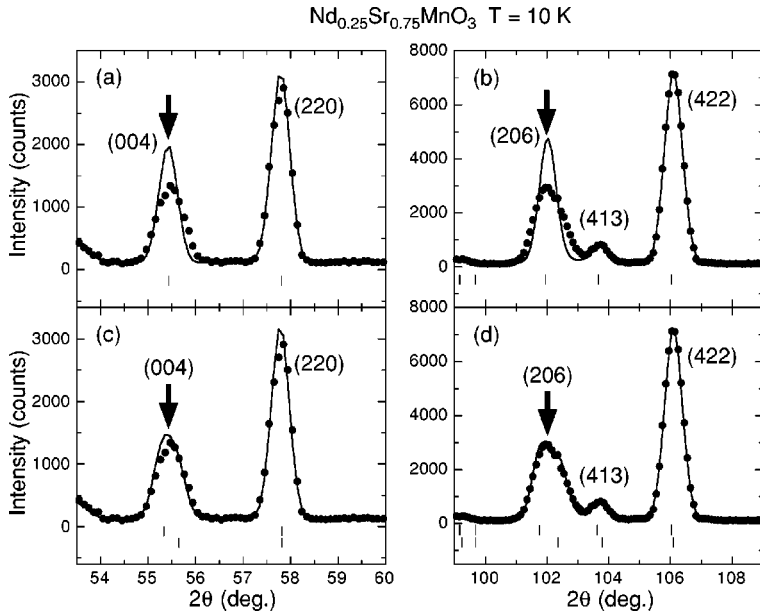
FIG. 9. Portions of the powder diffraction pattern of the $x=0.75$ sample at 10 K. The solid lines represent the calculated intensity obtained from the Rietveld analysis. The calculated peak positions are indicated as vertical bars. (a),(b) The refinement was performed assuming a single phase of the space group $I4/mcm$. (c),(d) The refinement was performed with two-phase model described in the text.

It is of interest to stress that we have observed a selective broadening of the nuclear Bragg reflections. Figure 8 represents the temperature dependence of the peak widths [full width at half maximum (FWHM)] of the (004) and (220) reflections for $x=0.75$, 0.70, and 0.67. The width of the (220) reflection remains constant throughout all temperatures. However, it is clear that the width of the (004) peak gradually increases below $T \sim T_N$. Note that the (004) reflection is attributed solely to nuclear reflection, and no magnetic scattering contributes to this reflection. Comparing the data for three samples depicted in Fig. 8, one can see that this peak broadening is more evident for $x=0.75$ and that it becomes less distinct as x decreases.

We have examined the powder diffraction patterns and have found that the broadening was limited to the reflections with the Miller indices (hkl) of large l, for example, (004), (114), (206), (226), and (008). In Fig. 9, we show typical examples of the broadening of the Bragg profiles for the $x=0.75$ sample at 10 K. The full circles are the observed intensity profiles and the solid lines are the calculated intensities obtained from the Rietveld refinement. One can clearly see that the (004) and (206) reflections are broader than those of (220) and (422). We first fitted the profile assuming that the sample consists of a single phase with the $I4/mcm$ symmetry, and the calculated profiles are depicted in Figs. 9(a) and (b). We can see that despite the fact that the fitting is quite good for (220) and (422), the fit for the (004) and (206) reflections is relatively poor.

Because the calculated peak positions are in excellent agreement with the observed peaks, the symmetry $I4/mcm$ assumed in our analysis cannot be too far from the true crystal symmetry. One possible reason for the observed broadening could be the lowering of symmetry to an orthorhombic or to a monoclinic structure, with a resulting splitting of reflections that may be unresolved due to the instrumental resolution. This possibility, however, can be easily discarded because the peak broadening is also observed at $(00l)$ reflections where no splitting is expected in the orthorhombic or monoclinic structures.

Considering that the peak broadening occurs selectively at the reflections with large l (i.e., the reflections from the lattice planes which are nearly perpendicular to the c axis), it is likely that it originates from an anisotropic strain in the system. A possible microscopic picture of such a strain involves a distribution of values of the lattice constant c. To test this idea, we have assumed a simple structural model in which the sample consists of two phases with two different c lattice constants. By keeping the other parameters identical for both phases we repeated the fit and found that this model substantially improves the results as depicted in Figs. 9(c) and (d).

From these facts, we concluded that the observed selective broadening of Bragg peaks results from the anisotropic strain caused by a distribution of the $d(3z^2-r^2)$ orbitals. As stated above, in the $O^{\ddagger}$ phase the e_g electrons occupy the $d(3z^2-r^2)$ orbitals. When the charges are localized in the insulating phase, only the Mn^{3+} sites have the $d(3z^2-r^2)$ orbital (the Mn^{4+} sites have no e_g electrons). In Fig. 10 we illustrate an arrangement of Mn^{3+} with the $d(3z^2-r^2)$ orbital and Mn^{4+} with no e_g orbital. Because the $d(3z^2-r^2)$ orbital extends toward the c direction, the distance between Mn^{3+} and Mn^{4+} is elongated along the c direction, whereas in the ab plane the Mn^{3+}-Mn^{4+} distance is almost equal to the Mn^{4+}-Mn^{4+} distance. At high temperatures the charges are mobile by thermal activation, a process that averages out the local distortion of the lattice spacing along the c axis. At low temperatures, on the other hand, the thermal energy is insufficient for the charges to hop, and the local ordering of
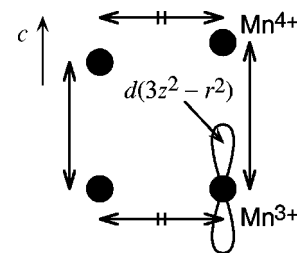

FIG. 10. Schematic picture of the relationship between e_g orbital ordering and the lattice spacing in the $O^{\ddagger}$ phase.

the e_g electrons with the $d(3z^2-r^2)$ orbital may be formed, leading to the anomaly in the lattice constant. It should be noted that the broadening of the peak starts below T_N where the C-type AFM spin ordering is formed as shown in Fig. 8, and where the temperature derivative of the resistivity also shows an anomaly.[12]

B. Possibility of the $x=0.8$ charge ordering in the C-type AFM phase

As we described in the previous subsection, we found that the broadening of the nuclear Bragg peaks becomes more evident as x increases, indicating that the charge localization/ordering is also progressively stabilized with the increase of x. Furthermore, the anomaly of the temperature derivative of the resistivity at T_N also develops as x increases, and it is most clearly observed at $x=0.80$. The resistivity of the $x=0.80$ sample also shows a steep increase at T_N upon cooling.[12] Judging from these facts, it is very likely that the charge ordering associated with the $Mn^{3+}:Mn^{4+}$ ratio of 1:4 is formed below T_N. We note that Jirák *et al.* have reported superlattice reflections which may originate from the charge ordering of $Mn^{3+}:Mn^{4+}=1:3$ in a $Pr_{0.2}Ca_{0.8}MnO_3$ sample where the valence distribution of the Mn ions was determined to be $Mn_{0.25}^{3+}Mn_{0.75}^{4+}$ by chemical analysis.[3] We examined our powder pattern profiles in detail, but it was not possible to detect any indication of any superlattice reflections that may be related to charge ordering. A study of a single-crystal sample would be strongly desirable to elucidate the nature of a possible 4/5 or 3/4 charge ordering in the C-type AFM phase.

As for the charge ordering for $x \geq 1/2$, an interesting charge ordering with a large periodicity was recently observed in the $La_{1-x}Ca_xMnO_3$ system.[32–36] In this system, incommensurate superlattice peaks were observed at the wave vector $Q=(\delta,0,0)$ with $\delta \sim 1-x$ below the charge ordering temperature T_{CO} by electron diffraction. To understand the incommensurability, a stripe-type charge/orbital ordering was proposed.[4,35,36] In this model, a pair of $Mn^{3+}O_6$ stripes are formed, and they are separated by another stripe-shaped region of the $Mn^{4+}O_6$ octahedra. The pair of $Mn^{3+}O_6$ stripes is accompanied by a $d(3x^2-r^2)/d(3y^2-r^2)$ orbital ordering and by a large lattice contraction due to the JT effect, while the $Mn^{4+}O_6$ regions are free from lattice distortions. At $x=1/2$, these incommensurate pairs of JT stripes converge to the well-known CE-type orbital/spin ordering. Similar incommensurate superlattice peaks were also observed in $Bi_{1-x}Ca_xMnO_3$ single crystals with $0.74 \leq x \leq 0.82$,[37] where a long-period structure, with fourfold periodicity (21 Å) and 32-fold periodicity (170 Å) of the orthorhombic lattice unit, was clearly observed in the $x=0.80$ sample.[38] These results also share many features with the paired JT stripes proposed for the $La_{1-x}Ca_xMnO_3$ with $x \gtrsim 0.5$.

We would like to point out that, from an analysis of the lattice parameters, we can easily exclude the possibility of this type of paired JT stripe ordering in the C-type AFM $Nd_{1-x}Sr_xMnO_3$ samples. For the CE-type charge ordering and associated paired JT stripe ordering, the orthorhombic c axis (in the $Pbnm$ notation) must be the shortest. This is due to the fact that the $d(3x^2-r^2)/d(3y^2-r^2)$ orbitals lie in the

ab plane as shown in Fig. 4. This can be easily checked in other manganites that exhibit CE-type ordering, as in $Pr_{1-x}Ca_xMnO_3$ (Refs. 3, 21, and 39) as well as in $La_{1-x}Ca_xMnO_3$ with $x \geq 0.50$ (Refs. 1, 40, and 41).

On the other hand, the c axis is the longest for the C-type AFM phase in $Nd_{1-x}Sr_xMnO_3$, in $Pr_{1-x}Ca_xMnO_3$ (Ref. 3), and in $La_{0.2}Ca_{0.8}MnO_3$ (Ref. 1). As explained above this relation of the lattice parameters results from the $d(3z^2-r^2)$-type orbital ordering in the C-type structure. In the case of $Bi_{1-x}Ca_xMnO_3$, we are puzzled that the magnetic ordering was reported to be of the C type.[37] As the c axis is expected to be the longest for the C-type structure, this type of spin ordering is incompatible with the proposed JT stripe-type ordering in which the c axis is the shortest.

Finally, we comment that the FWHM of the (004) peak of the $x=0.75$ sample at 330 K is larger than the one at about 300 K (see Fig. 8). This is because a finite amount of the scattering exists between the (220) and (004) peaks. Similar extra scattering is also observed at other scattering angles. Presumably, another phase with lattice parameters a and c of very similar lengths may exist at higher temperature than 330 K, and this high-temperature phase may coexist at 330 K with the described $O^\ddagger$ phase.

VII. CONCLUSIONS

A neutron diffraction study was performed on $Nd_{1-x}Sr_xMnO_3$ powder samples with $0.49 \leq x \leq 0.75$. Their crystal and magnetic structures were analyzed by the Rietveld method. A systematic change of the crystal and magnetic structures was observed as a function of x. With increasing x, the magnetic structure of the ground state varies from metallic ferromagnetism to charge-ordered CE-type antiferromagnetism, to metallic A-type antiferromagnetism, and finally to insulating C-type antiferromagnetism. The magnetic structures can be interpreted to be driven by underlying Mn e_g orbital ordering, and their resultant crystal structures. In the CE-type and A-type AFM states, the crystal structure is characterized by apically compressed MnO_6 octahedra reflecting the planar $d(x^2-y^2)$-type orbital ordering. On the other hand, the crystal structure of the C-type AFM state is characterized by apically elongated octahedra resulting from the ordering of the rod-type $d(3z^2-r^2)$ orbitals.

The CE-type AFM state was observed only in the neighborhood of $x=1/2$. In the $x=0.51$ sample, the CE-type AFM and the A-type AFM states coexist due to the small energy difference between these two AFM states. In addition, the C-type AFM phase exhibits an anisotropic broadening of Bragg peaks, which becomes more evident as x increases. This broadening may be a precursor of the $d(3z^2-r^2)$-type orbital ordering at $Mn^{3+}:Mn^{4+}=1:3$ or 1:4.

*Present address: Dept. of Physics, Faculty of Science, Ochanomizu University, Bunkyo-ku, Tokyo 112-8610, Japan.

†Present address: Faculty of Science and Technology, Sophia University, Chiyoda-ku, Tokyo 102-8554, Japan.

‡Present address: Faculty of Engineering, Yamagata University, Yonezawa, Yamagata 990-8510, Japan.

[1] E. O. Wollan and W. C. Koehler, Phys. Rev. **100**, 545 (1955).

[2] J. B. Goodenough, Phys. Rev. **100**, 564 (1955).

[3] Z. Jirák, S. Krupička, Z. Šimša, M. Dlouhá, and S. Vratislav, J. Magn. Magn. Mater. **53**, 153 (1985).

[4] S-W. Cheong and C. H. Chen, in *Colossal Magnetoresistance, Charge Ordering and Related Properties of Manganese Oxides*, edited by C. N. R. Rao and B. Raveau (World Scientific, Singapore, 1998), p. 241.

[5] R. Maezono, S. Ishihara, and N. Nagaosa, Phys. Rev. B **57**, R13 993 (1998); **58**, 11 583 (1998).

[6] T. Mizokawa and A. Fujimori, Phys. Rev. B **56**, R493 (1997).

[7] W. Koshibae, Y. Kawamura, S. Ishihara, S. Okamoto, J. Inoue, and S. Maekawa, J. Phys. Soc. Jpn. **66**, 957 (1997).

[8] H. Kawano, R. Kajimoto, H. Yoshizawa, Y. Tomioka, H. Kuwahara, and Y. Tokura, Phys. Rev. Lett. **78**, 4253 (1997); H. Kawano, R. Kajimoto, H. Yoshizawa, J.A. Fernandez-Baca, Y. Tomioka, H. Kuwahara, and Y. Tokura, Physica B **241-243**, 289 (1998).

[9] H. Yoshizawa, R. Kajimoto, H. Kawano, J. A. Fernandez-Baca, Y. Tomioka, H. Kuwahara, and Y. Tokura, Mater. Sci. Eng. B **63**, 125 (1999); H. Kawano, R. Kajimoto, H. Yoshizawa, Y. Tomioka, H. Kuwahara, and Y. Tokura, cond-mat/9808286 (unpublished).

[10] H. Kuwahara, Y. Tomioka, A. Asamitsu, Y. Moritomo, and Y. Tokura, Science **270**, 961 (1995).

[11] H. Kuwahara, T. Okuda, Y. Tomioka, A. Asamitsu, and Y. Tokura, Phys. Rev. Lett. **82**, 4316 (1999).

[12] H. Kuwahara, T. Okuda, Y. Tomioka, A. Asamitsu, and Y. Tokura, in *Science and Technology of Magnetic Oxides*, edited by M. Hundley, J. Nickel, R. Ramesh, and Y. Tokura, MRS Symposia Proceedings No. 494 (Materials Research Society, Pittsburgh, 1998), p. 83; (unpublished).

[13] H. Kuwahara, Y. Moritomo, Y. Tomioka, A. Asamitsu, M. Kasai, R. Kumai, and Y. Tokura, Phys. Rev. B **56**, 9386 (1997).

[14] F. Izumi, in *The Rietveld Method,* edited by R. A. Young (Oxford University Press, Oxford, 1993), Chap. 13; Y.-I. Kim and F. Izumi, J. Ceram. Soc. Jpn. **102**, 401 (1994).

[15] Although the relation of the *a* and *b* parameters is reverse to the definition in Ref. 3, we shall call this structure as O' structure in this paper.

[16] Z. Jirák, E. Pollert, A. F. Andersen, J.-C. Grenier, and P. Hagenmuller, Eur. J. Solid State Inorg. Chem. **27**, 421 (1990).

[17] V. Caignaert, F. Millange, M. Hervieu, E. Suard, and B. Raveau, Solid State Commun. **99**, 173 (1996).

[18] J. Wolfman, A. Maignan, Ch. Simon, and B. Raveau, J. Magn. Magn. Mater. **159**, L299 (1996).

[19] A. Sundaresan, P. L. Paulose, R. Mallik, and E. V. Sampathkumaran, Phys. Rev. B **57**, 2690 (1998).

[20] A. M. Glazer, Acta Crystallogr., Sect. A: Cryst. Phys., Diffr., Theor. Gen. Crystallogr. **A31**, 756 (1975).

[21] H. Yoshizawa, H. Kawano, Y. Tomioka, and Y. Tokura, Phys. Rev. B **52**, R13 145 (1995); J. Phys. Soc. Jpn. **65**, 1043 (1996).

[22] R. Kajimoto, T. Kakeshita, Y. Oohara, H. Yoshizawa, Y. Tomioka, and Y. Tokura, Phys. Rev. B **58**, R11 837 (1998).

[23] D. E. Cox, P. G. Radaelli, M. Marezio, and S-W. Cheong, Phys. Rev. B **57**, 3305 (1998).

[24] T. Akimoto, Y. Maruyama, Y. Moritomo, A. Nakamura, K. Hirota, K. Ohoyama, and M. Ohashi, Phys. Rev. B **57**, R5594 (1998).

[25] Y. Moritomo, T. Akimoto, A. Nakamura, K. Ohoyama, and M. Ohashi, Phys. Rev. B **58**, 5544 (1998).

[26] Close inspection of the crystal structures of the *CE*-type samples and the *A*-type $x=0.55$ sample leads one to notice that there is no significant difference of the structural parameters except a smooth variation as a function of *x*.

[27] H. Yoshizawa, H. Kawano, J. A. Fernandez-Baca, H. Kuwahara, and Y. Tokura, Phys. Rev. B **58**, R571 (1998).

[28] As far as the diffraction condition is concerned, it is possible that the canting angle is 0°. However, from the value of the magnetic moments listed in Table I, 0° canting angle implies the abnormal moment distribution of $\sim 4\mu_B$ and $\sim 0.9\mu_B$, and it is very unlikely.

[29] B. J. Sternlieb, J. P. Hill, U. C. Wildgruber, G. M. Luke, B. Nachumi, Y. Moritomo, and Y. Tokura, Phys. Rev. Lett. **76**, 2169 (1996).

[30] M. Kubota, H. Yoshizawa, Y. Moritomo, H. Fujioka, K. Hirota, and Y. Endoh, J. Phys. Soc. Jpn. **68**, 2202 (1999).

[31] We noticed that the profiles of several peaks are broad and asymmetric.

[32] A. P. Ramirez, P. Schiffer, S-W. Cheong, C. H. Chen, W. Bao, T. T. M. Palstra, P. L. Gammel, D. J. Bishop, and B. Zegarski, Phys. Rev. Lett. **76**, 3188 (1996).

[33] C. H. Chen and S.-W. Cheong, Phys. Rev. Lett. **76**, 4042 (1996).

[34] C. H. Chen, S-W. Cheong, and H. Y. Hwang, J. Appl. Phys. **81**, 4326 (1997).

[35] S. Mori, C. H. Chen, and S-W. Cheong, Nature (London) **392**, 473 (1998).

[36] S. Mori, C. H. Chen, and S-W. Cheong, Phys. Rev. Lett. **81**, 3972 (1998).

[37] W. Bao, J. D. Axe, C. H. Chen, and S-W. Cheong, Phys. Rev. Lett. **78**, 543 (1997).

[38] Y. Murakami, D. Shindo, H. Chiba, M. Kikuchi, and Y. Syono, Phys. Rev. B **55**, 15 043 (1997).

[39] M. R. Lees, J. Barratt, G. Balakrishnan, D. McK. Paul, and C. Ritter, Phys. Rev. B **58**, 8694 (1998).

[40] P. G. Radaelli, D. E. Cox, M. Marezio, and S-W. Cheong, Phys. Rev. B **55**, 3015 (1997); P.G. Radaelli, D.E. Cox, L. Capogna, S-W. Cheong, and M. Marezio, *ibid.* **59**, 14 440 (1999).

[41] M. R. Ibarra, J. M. De Teresa, J. Blasco, P. A. Algarabel, C. Marquina, J. Garcia, J. Stankiewicz, and C. Ritter, Phys. Rev. B **56**, 8252 (1997).